Enzyme-like reactivity for increasing selectivity in CO_2 electrochemical reduction

Adarsh Koovakattil Surendran,[‡] Guilherme L. Tripodi,[‡] Eva Pluhařová,[⊥] Aleksandr Y. Pereverzev,[‡] Jeroen P. J. Bruekers,[‡] Johannes A. A. W. Elemans,[‡] Evert Jan Meijer,[†] and Jana Roithová,[‡]*

[‡]Institute for Molecules and Materials, Radboud University, Heyendaalseweg 135, 6525 AJ Nijmegen, The Netherlands.

[⊥]J. Heyrovský Institute of Physical Chemistry, v.v.i., The Czech Academy of Sciences, Dolejškova 2155/3, 182 23 Prague, Czech Republic

[†]Van 't Hoff Institute for Molecular Sciences and Amsterdam Center for Multiscale Modelling, University of Amsterdam, Science Park 904, 1098 XH, Amsterdam, The Netherlands.

ABSTRACT: The development of selective catalysts for the reduction of CO_2 mostly focuses on electrocatalytic approaches and aims at increasing the selectivity of the reaction while keeping a high activity, which is difficult to achieve. Metalloporphyrins are good catalysts for CO_2 reduction because they have favorable electronic properties and offer the possibility to make use of secondary coordination sphere effects. Here, we present a new approach to CO_2 reduction, which is based on host-guest chemistry enabled by an iron porphyrin cage catalyst. When this iron porphyrin cage catalyst is immobilized on a conducting carbon support the selectivity for CO_2 reduction to CO stays above 90 % in a wide range of overpotentials. The hosting of potassium ions in the cage of the catalyst decreases the overpotential of the reduction and increases the catalytical activity while retaining the high selectivity. DFT calculations show that the potassium ions assist the reduction of CO_2 by making the 2-electron transfer from iron(0) to CO_2 exothermic. Upon protonation, the Fe-COOH intermediates have been trapped by combining an electrochemical cell with an electrospray ionization mass spectrometer and their structure has been characterized by cryogenic ion spectroscopy.

INTRODUCTION

One of the current most pressing scientific challenges is the development of selective catalysts for the reduction of CO_2, which would enable us to process CO_2 more efficiently and at smaller costs.[1–3] Electrocatalytic CO_2 reduction seems to be the most promising direction[4–6] and many catalysts are currently being developed.[7–12] Optimization of their structures has led to impressively improved properties,[13–17] but the low selectivity with regard to undesired side reactions, such as hydrogen evolution, remains problematic. For a solution to this problem one may take an inspiration from enzymatic reactions, which excel in selectivity and often also in activity.[18,19] Enzymes achieve this by binding and transforming substrates in optimized reaction pockets.[20] Hence, the design of synthetic catalysts should also take advantage of 3D constrained reaction sites, while keeping optimizing of the electronic properties of the catalytic center(s).[21–24]

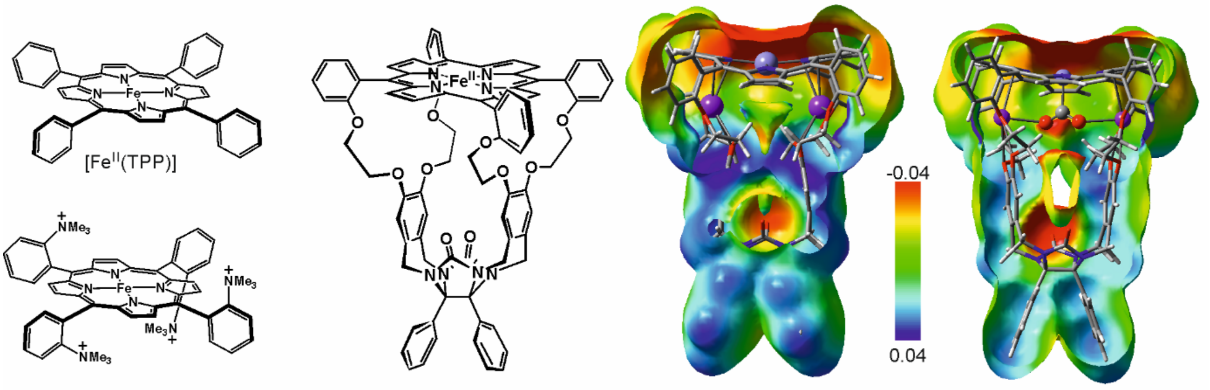

[Fe^{II}(o-TMA)]$^{4+}$ [(**1**)Fe^{II}] [(**1**)Fe^{0}K$_2$] [(**1**)Fe(CO$_2$)K$_2$]

Figure 1. (a) Iron tetraphenylporphyrin [Fe^{II}(TPP)] and [Fe^{II}(o-TMA)]$^{4+}$, which so far is the best iron porphyrin catalyst for the electrochemical reduction of CO_2.[25] (b) Iron cage catalyst [(**1**)Fe^{II}]. (c) Right: electrostatic potentials mapped on the electron isodensity surface (0.001) of the DFT-optimized structures of [(**1**)Fe^{0}K$_2$] and [(**1**)FeK$_2$(CO$_2$)] (see the theoretical details). The backbone of the porphyrin cage catalyst is shown in the stick representation, the positions of the metals (Fe, K) and O-C-O are highlighted by the ball-and-stick representation. The surface is clipped from the front to show the electrostatic potential inside the cavity.

Metalloporphyrin cages may be used to model enzymatic reactions involving heme reaction centers.[26] At the same time, porphyrins are among the most extensively studied catalysts for CO_2 reduction.[27] The systematic variation of the porphyrin backbone has converged to the currently best performing catalyst, which is an iron tetraphenylporphyrin possessing permanently charged ammonium groups near the central metal atom (Figure 1a).[25,28,29] Here, we go one step further and add to this design the constrained space of a diphenylglycoluril-based cage, which acts as a secondary sphere ligand to the iron center[30] (compound [(**1**)Fe^{II}], see Figure 1b). Iron porphyrin catalysts used for the reduction of CO_2 are active in the iron(0) oxidation state making the catalyst doubly negatively charged. Cage catalyst [(**1**)Fe^{II}] has a glycoluril framework with the sidewalls linked to the metalloporphyrin via oxyethyleneoxy spacers that can serve as crown-ether-like coordination sites for alkali metal ions. Preliminary force-field molecular dynamics simulations of aqueous systems confirm that in particular potassium is well positioned in the sidewalls (Figures S25 and S26). DFT calculated electrostatic potential of the iron cage shows a polarized reaction pocket that might assist in the reduction of CO_2 (Figure 1c, see SI for the computational details). Hence, this suggests that the system represents a perfect case for exploring the effect of a reaction pocket on the CO_2 reduction.

RESULTS AND DISCUSSION

We investigated the effect of the cage cavity on CO_2 reduction and the possibility to tune the electrostatic potential by hosting alkali metals first by homogeneous electrocatalysis. The host-guest interactions between the cage catalyst and cations can be studied by adding various electrolytes containing different cations. We compared the effect of electrolytes containing K^+ (KBF_4 in DMF/H_2O), Na^+ ($NaBF_4$ in DMF/H_2O), and TBA^+ ($TBABF_4$ in DMF/H_2O, TBA = *n*-Bu_4N). Potassium and sodium ions can coordinate to the oxyethylenoxy units of the catalyst, whereas the TBA^+ ions are too bulky to coordinate. Hence, in the presence of the latter ions we can monitor the catalytic reactivity of the cage catalyst without the charged cavity.

Cyclic voltammetry of the [(**1**)Fe] solutions under a nitrogen atmosphere (Figure 2a) shows that the redox potential of the $Fe^{2+} \rightarrow Fe^+$ transition is almost unaffected by the cations of the electrolyte. However, the catalytically important $Fe^+ \rightarrow Fe^0$ transition is sensitive to the presence of the alkali metals (compare the blue/gray/orange curves in in Figure 2a). Changing the electrolyte cations from TBA^+ to Na^+ or K^+ resulted in an over-potential shift of 75 mV and 260 mV ($E_{1/2}$, Figure S3), respectively, attesting that the alkali metals change the electronic properties of the cage catalyst and that the effect of the potassium ions is particularly strong. The electrochemistry results alone do not reveal, whether the [(**1**)Fe^0] complex interacts with one or two potassium (sodium) ions (i.e., [(**1**)$Fe^0K]^-$ or [(**1**)Fe^0K_2]), both is possible. For comparison, the same experiments with the simple tetraphenyl porphyrin iron catalyst [Fe(TPP)] did not show any overpotential shift (Figure S3 in the Supporting Information).

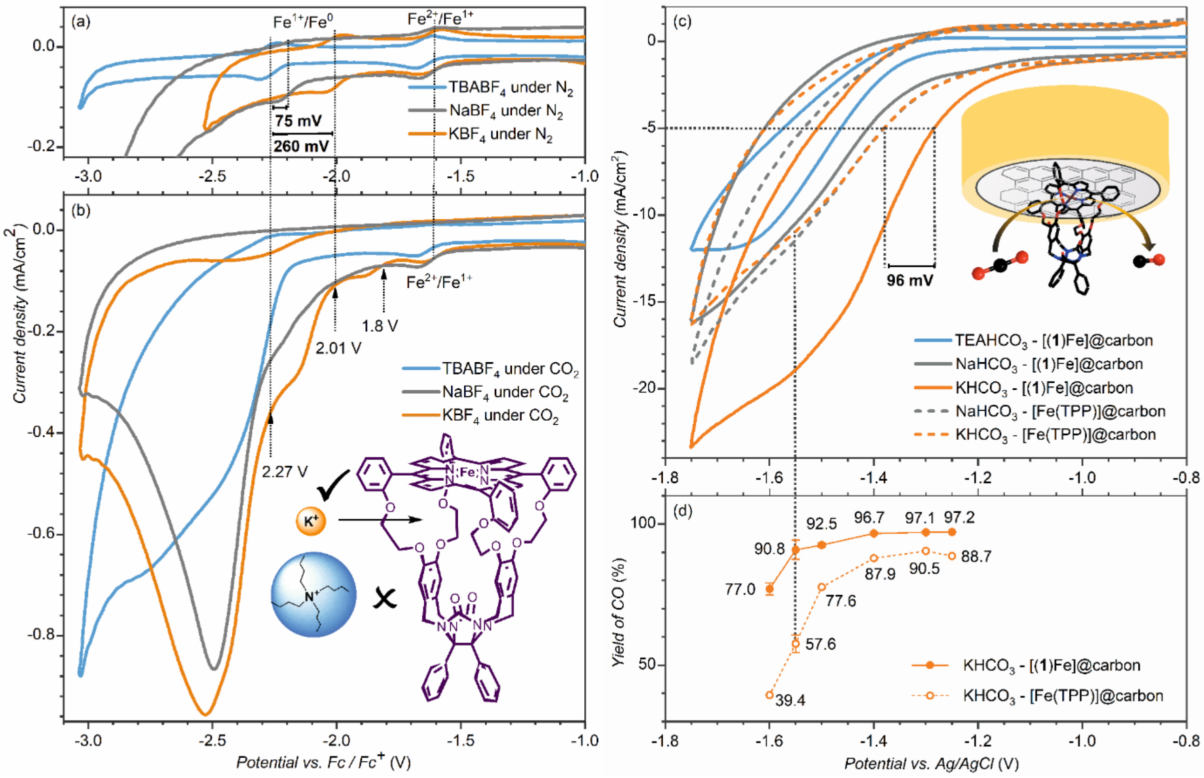

Figure 2. Left: Homogeneous cyclic voltammetry (CV) of [(**1**)Fe] (0.25mM) measured in electrolytes containing $TBABF_4$ (blue), $NaBF_4$ (grey), and KBF_4 (orange) (0.1 M in DMF + 0.5M H_2O; scan rate 100 mV/s) under (a) N_2 and (b) CO_2. Right: (c) Heterogeneous cyclic voltammetry of immobilized [(**1**)Fe]@carbon (solid lines) and [Fe(TPP)]@carbon (dashed lines) in $TEAHCO_3$ (blue), $NaHCO_3$ (grey), $KHCO_3$ (orange) electrolytes (0.5 M in H_2O) under CO_2. (d) Selectivity of the CO formation in the CO_2RR catalyzed by [(**1**)Fe]@carbon (full points) and [Fe(TPP)]@carbon (open points) in 0.5 M aqueous solution of $KHCO_3$ under CO_2.

Under the CO_2 atmosphere, an increased current wave at the $Fe^+ \rightarrow Fe^0$ potential was observed corresponding to the catalytic CO_2 reduction reaction (CO_2RR; compare blue lines in Figure 2a and 2b for CO_2RR in the TBA^+ electrolyte). In the presence of potassium ions, three waves beyond the $Fe^{2+} \rightarrow Fe^+$ reduction were detected. The first wave (-1.8 V vs. Fc) occurred before the $Fe^+ \rightarrow Fe^0$ reduction detected under the N_2 atmosphere (compare Figure 2a and 2b). This process could be a result of the binding of CO_2 to the $[(\mathbf{1})Fe^{I}]^-$ complex hosting potassium ion(s) that could be then reduced to iron(0) at a lower overpotential. The second current increase is at the detected $Fe^+ \rightarrow Fe^0$ reduction potential (-2.01 V) and thus corresponds to the CO_2 reduction reaction with a complex hosting the potassium ion(s). Finally, the CO_2RR proceeds also at the $Fe^+ \rightarrow Fe^0$ reduction potential detected in the TBA^+-based electrolyte (~-2.27 V) representing the catalysis by the bare $[(\mathbf{1})Fe^{I}]^-$ catalysts without the guest potassium ions. The catalytic current for the CO_2RR at -2.01 V is smaller than that observed at -2.27 V. The kinetic hindrance of the CO_2RR catalyzed by the cage catalyst hosting potassium ion(s) can be due to the stabilization of an intermediate by the interaction with potassium ions, kinetic hindrance of proton transfer reactions, or due to different diffusion properties of the cage catalysts with and without the potassium guests. The results with the sodium-based electrolyte also suggest an effect of cage-sodium host-guest chemistry on the CO_2RR, but the effect is weaker than for that of the cage-potassium host-guest chemistry.

The diffusion limitation of the catalysis can be overcome by immobilization of the porphyrin cage catalysts onto a support.[31] At the same time, this immobilization allows the use of aqueous electrolytes which removes a possible kinetic bottleneck of the accompanying proton-transfer reactions[32–34] Therefore, we immobilized the cage catalyst onto an inert vulcanized conducting carbon support (see the optimization procedure and the details of the process in the Supporting Information) and performed the experiments in 0.5 M aqueous solutions of $TEAHCO_3$, $NaHCO_3$, and $KHCO_3$, respectively. The comparison of the cyclic voltammetry experiments in different electrolytes shows that the host-guest chemistry also works for the immobilized [(**1**)Fe]@carbon catalyst in analogy to the homogeneous catalysis experiments (Figure 2c). Compared to the experiments with the electrolyte containing the non-coordinating TEA^+, the use of Na^+ or K^+ based electrolytes reduced the onset potential by ~22 mV and by ~110 mV, respectively (Figure S8). To our delight, the catalytic activity at the reduced potentials was not suppressed, but instead enhanced (Figure 2c).

The CO_2RR catalytic activity is usually larger in the presence of the alkali metal-based electrolytes than in the presence of the ammonium-based electrolytes, regardless of whether the catalyst is immobilized or not.[35,36] Therefore, we decided to assess the inherent effect of the electrolyte by comparing the results obtained for the [(**1**)Fe]@carbon catalyst with the results for the reference [Fe(TPP)]@carbon catalyst under the same conditions. The onset potentials for the CO_2RR catalyzed by [Fe(TPP)]@carbon were the same in all studied electrolytes (Figures S7 and S8). As expected, the catalytic activity of [Fe(TPP)]@carbon in alkali-metal based electrolyte solutions was larger than that in solutions containing the $TEAHCO_3$ electrolyte (Figures S7 and S8). However, there is no significant difference between the $NaHCO_3$ and $KHCO_3$ electrolyte solutions (compare the dashed lines in Figure 2c). Hence, the significantly increased catalytic activity of the cage catalyst [(**1**)Fe]@carbon in the presence of the $KHCO_3$-based electrolyte (as compared to the $NaHCO_3$-based electrolyte) is most likely the result of the tuning of the catalyst by host-guest interactions. In addition, the overpotential for CO_2RR with the [(**1**)Fe]@carbon catalyst in the $KHCO_3$-based electrolyte is shifted by 96 mV with respect that of the [Fe(TPP)]@carbon catalyst demonstrating the modified electronic properties of the cage catalyst hosting the potassium ions.

The selectivity of catalysts is often considered to be even more important than their activity. The CO_2RR catalyzed by porphyrin-based catalysts usually yield CO along with the undesired evolution of H_2. We compared the selectivity of the [(**1**)Fe]@carbon catalyst for the production of CO with the selectivity of the [Fe(TPP)]@carbon catalyst in the presence of either $TEAHCO_3$ or $KHCO_3$ as the electrolyte salts (Figure S10 and Figure 2d, respectively). The CO : H_2 selectivity of the [(**1**)Fe]@carbon catalyst was above 90% for potentials up to -1.55 V vs. Ag/AgCl in both electrolytes and this selectivity was always higher than that of [Fe(TPP)]@carbon. Quantitative bulk experiments at -1.55 V in the presence of $KHCO_3$-based electrolyte showed circa 90% Faradaic efficiency for CO formation with [(**1**)Fe]@carbon and only circa 50% Faradaic efficiency with [Fe(TPP)]@carbon. Hence, these results clearly indicate that the cage catalyst achieves a high CO selectivity in CO_2RR and this selectivity is retained also after boosting the activity by hosting the potassium ions.

In order to get a deeper insight into the host-guest chemistry of the cage catalyst and into the mechanism of the CO_2 reduction reaction, we studied the intermediates in the electrochemical reaction by electrospray ionization mass spectrometry (ESI-MS).[37] Transferring the intermediates by electrospray ionization into a mass spectrometer is a challenging task,[38–40] because these intermediates are formed at the cathode and presumably are short-lived and thus extremely low abundant in solution.[41] In addition, the reduced reactive species can be oxidized and thus be destroyed during the electrospray ionization process. Nevertheless, an optimized design of an electrochemical cell consisting of a carbon working electrode, a stainless-steel counter electrode, and a Pt wire pseudo-reference electrode controlled by a floating potentiostat assembly (see the Supporting Information) enabled us to detect the desired reduced species (Figure 3). The electrochemically formed complexes are transferred by a silica capillary that is sandwiched in between two carbon sheets of the working electrode directly connected to the electrospray ionization source of a mass spectrometer.

The reference ESI-MS spectrum of an acetonitrile solution of $[(\mathbf{1})\mathrm{Fe}^{\mathrm{III}}\mathrm{Cl}]$ and KBF_4 showed one dominant signal for $[(\mathbf{1})\mathrm{Fe}^{\mathrm{III}}(\mathrm{Cl})\mathrm{K}]^+$ (Figure 3a). After applying a negative voltage (-3 V), the signal of $[(\mathbf{1})\mathrm{Fe}^{\mathrm{III}}(\mathrm{Cl})\mathrm{K}]^+$ depleted and the spectra showed the formation of $\mathrm{Fe}^{\mathrm{II}}$ complexes in the positive mode and Fe^{I} complexes in the negative mode (Figure 3 and Figure S15, respectively). The reactive Fe^0 complexes should be either neutral $[(\mathbf{1})\mathrm{Fe}^0\mathrm{K}_2]$ or anionic $[(\mathbf{1})\mathrm{Fe}^0\mathrm{K}]^-$ and $[(\mathbf{1})\mathrm{Fe}^0]^{2-}$species. The neutral complexes cannot be detected by mass spectrometry and the reactive anions likely lose electrons easily during the ionization process[42]to form the detected $[(\mathbf{1})\mathrm{Fe}^{\mathrm{I}}]^-$. Therefore, their absence in the spectra is not surprising. After saturation of the solution with CO_2, new complexes appeared (see color-highlighted signals in Figures 3b and 3c). The detected intermediates contain the CO_2H group and correspond to positively charged $[(\mathbf{1})\mathrm{Fe}^{\mathrm{II}}(\mathrm{CO_2H})\mathrm{K}_2]^+$ and negatively charged $[(\mathbf{1})\mathrm{Fe}^{\mathrm{II}}(\mathrm{CO_2H})]^-$. These intermediates are formed by the reaction of either $[(\mathbf{1})\mathrm{Fe}^0\mathrm{K}_2]$ or $[(\mathbf{1})\mathrm{Fe}^0]^{2-}$, respectively, with CO_2, followed by protonation. Both complexes probably have a short life time and therefore can only be trapped at a low temperature (-40 °C). This is the first time that such intermediates in CO_2RR have been detected by mass spectrometry, which opens the possibility to study their unimolecular properties and their spectroscopic characteristics.

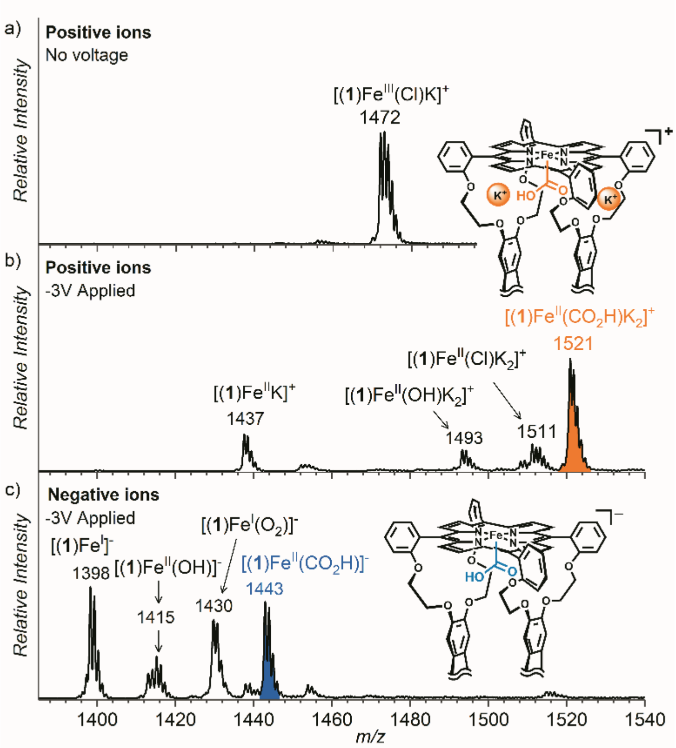

Figure 3. (a) EC-ESI-MS (electrochemistry – electrospray ionization mass spectrometry) spectra of an acetonitrile solution of $[(\mathbf{1})\mathrm{Fe^{III}Cl}]$ (0.143 mM) and $\mathrm{KBF_4}$ (0.150 mM) measured under the N_2 atmosphere without applying a voltage. (b,c) The same experiment but now under the CO_2 atmosphere at -40 °C with an applied voltage of -3 V (vs. Pt wire reference electrode) in the positive (b) and the negative (c) ion mode.

The collision-induced dissociation of the intermediates leads almost exclusively to the elimination of CO and the formation of the corresponding iron-hydroxo complexes $[(\mathbf{1})\mathrm{Fe^{II}(OH)K_2}]^+$ and $[(\mathbf{1})\mathrm{Fe^{II}(OH)}]^-$ (Figure S17). The bond dissociation energy (*BDE*) for the CO loss determined from energy-resolved experiments[43,44] amounts to 1.29 ± 0.05 eV for $[(\mathbf{1})\mathrm{Fe^{II}(CO_2H)K_2}]^+$ and to 1.24 ± 0.10 eV for $[(\mathbf{1})\mathrm{Fe^{II}(CO_2H)}]^-$ (Figure S20). Hence, the hosting of the potassium ions in the cage does not significantly affect the energy demand of the rate-determining C-O bond cleavage (at least in the gas phase).[45,46] Although we can study this fragmentation only in the gas phase, the mass spectra of the complexes directly taken from solution suggest that the hydroxo complexes $[(\mathbf{1})\mathrm{Fe^{II}(OH)K_2}]^+$ and $[(\mathbf{1})\mathrm{Fe^{II}(OH)}]^-$ form in solution and only in the presence of CO_2 (cf. Figure 3 and Figures S15 and S16). Hence, the data are consistent with the pathway from the iron hydroxycarbonyl complexes to the hydroxo complexes. Frequently considered iron carbonyl intermediates were not detected under any experimental conditions.[47]

The structure of the isolated $[(\mathbf{1})\mathrm{Fe^{II}(CO_2H)K_2}]^+$ intermediate was characterized by cryogenic infrared photodissociation (IRPD) spectroscopy (Figure 4).[48–52] The interpretation of the spectrum of $[(\mathbf{1})\mathrm{Fe^{II}(CO_2H)K_2}]^+$ is based on a comparison with the IRPD spectra of the related $[(\mathbf{1})\mathrm{Fe^{II}K}]^+$ and $[(\mathbf{1})\mathrm{Fe^{II}(Cl)K_2}]^+$ complexes. The IRPD spectra of these reference ions differ in the position of the C-O stretching and CH_2 deformation vibrations of the crown ether-like moiety of the cage ligand and in the position of the urea carbonyl vibrations (see highlighted areas in Figure 4a). The urea carbonyl vibrations of $[(\mathbf{1})Fe^{II}K]^+$ are slightly red-shifted compared to those of $[(\mathbf{1})Fe^{II}(Cl)K_2]^+$, suggesting that the potassium ion in the $[(\mathbf{1})Fe^{II}K]^+$ complex is coordinated lower in the cavity in the vicinity of the carbonyl groups (see also a comparison with the spectrum of $[(\mathbf{1})Fe^{III}]^+$ in Figure S22). The differences in the crown ether-like moiety range suggest that the two potassium ions of $[(\mathbf{1})Fe^{II}(Cl)K_2]^+$ are likely coordinated to the oxyethyleneoxy functions attached to the sidewalls of the cage compound.

The IRPD spectrum of the $[(\mathbf{1})Fe^{II}(CO_2H)K_2]^+$ intermediate is almost identical to that of $[(\mathbf{1})Fe^{II}(Cl)K_2]^+$ attesting the same mode of potassium coordination, i.e. to the oxyethyleneoxy functions of the cage. The presence of the hydroxycarbonyl functionality is evidenced by the additional peaks in the IRPD spectrum of $[(\mathbf{1})Fe^{II}(CO_2H)K_2]^+$ in comparison to that of $[(\mathbf{1})Fe^{II}(Cl)K_2]^+$: the O-H vibration is at 3473 cm^{-1} and the C=O vibration at 1630 cm^{-1}. For comparison, the C=O vibration of the independently generated formate (O-coordinated carboxylate) complex $[(\mathbf{1})Fe^{II}(OCOH)K_2]^+$ is at 1638 cm^{-1} (Figure S12) and the CO frequency of a recently detected iron porphyrinoid hydroxycarbonyl in solution is 1682 cm^{-1}.[53] Our assignment was further corroborated by DFT calculations. The most stable isomer of $[(\mathbf{1})Fe^{II}(CO_2H)K_2]^+$ has its hydroxycarbonyl group coordinated to the iron center on the inside of the cage and this binding mode is stabilized by interactions between the oxygen atoms of the hydroxycarbonyl group and the potassium ions coordinated to the oxyethyleneoxy functions of the sidewalls (see Figures S21 and S23 for all DFT calculations in the gas phase). The theoretical IR spectrum reproduces all features in the experimental IRPD spectrum and attest the structure of the intermediate (Figure 4c). Alternative structures with different coordination of the potassium ions are less energetically favored and their IR spectra do not agree with the experimental one (Figure S21).

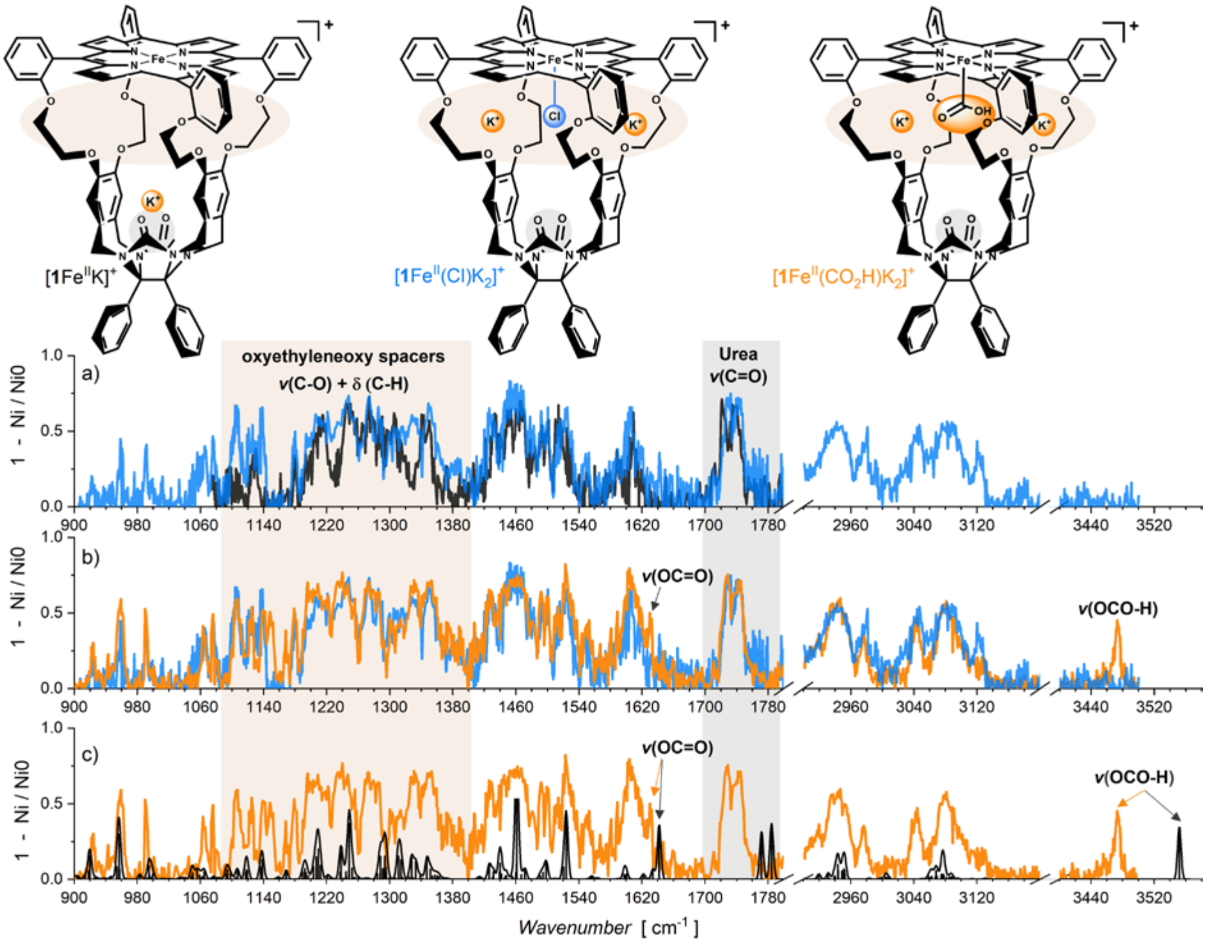

Figure 4. (a) IRPD spectra of the mass selected ions $[(\mathbf{1})Fe^{II}(Cl)K_2]^+$ (blue) and $[(\mathbf{1})Fe^{II}K]^+$ (black). (b) IRPD spectra of the mass selected ions $[(\mathbf{1})Fe^{II}(Cl)K_2]^+$ (blue) and $[(\mathbf{1})Fe^{II}(CO_2H)K_2]^+$ (orange). (c) Theoretical IR spectrum of gaseous $[(\mathbf{1})Fe^{II}(CO_2H)K_2]^+$ (black, B3LYP-D3/def2SVP; see also Figure S22) and the IRPD spectrum $[(\mathbf{1})Fe^{II}(CO_2H)K_2]^+$ (orange).

Finally, we explored the mechanism of the CO_2RR by DFT calculations (Figure 5). The calculations suggest that $[(\mathbf{1})Fe^0]^{2-}$ has a quintet ground state.[54,55] The complexation of CO_2 inside the cavity is associated with the spin change to the triplet state and is slightly endoergic. The C-binding of CO_2 to the iron center is associated with a 2-electron transfer from iron to CO_2 and leads to the singlet state $^1[(\mathbf{1})Fe(CO_2)]^{2-}$ complex that is protonated in a strongly exothermic step to form the detected intermediate $[(\mathbf{1})Fe(CO_2H)]^-$. We have approximated the protonation as a reaction with a protonated DMF molecule (other approaches would lead to slightly different values for the exothermicity of this step, but would not change the statement that this step is exothermic). Finally, the CO elimination leads to $[(\mathbf{1})Fe(OH)]^-$. This step is slightly endoergic and it is associated with a spin flip (the calculations predict the same energy for the triplet and the quintet state).

Introducing potassium cations in the cage stabilizes the triplet state as the ground state of the starting complex $[(\mathbf{1})Fe^0K_2]$. The complex binds CO_2 inside the cavity with both oxygen atoms weakly coordinating to the potassium ions and the process is exoergic. The electrostatic field of the potassium ions in ^{3}[(**1**)FeK$_2$(CO$_2$)] makes the following 2-electron reduction step towards the singlet state complex ^{1}[(**1**)FeK$_2$(CO$_2$)] exothermic, because the potassium ions stabilize the negative charge formed at the oxygen atoms (as also suggested in Figure 1). The subsequent protonation of the ^{1}[(**1**)FeK$_2$(CO$_2$)] intermediate is strongly exothermic and the final step of CO elimination is associated with a spin-flip to the quintet state and is endoergic. The comparison of both potential energy surfaces shows that the placing of the positively charged ions above the porphyrin plane inverts the key steps of the CO$_2$ reduction from endothermic to exothermic and thus explains a large activity of the cage catalyst [(**1**)Fe^{0}K$_2$] as well as of previously published [Fe^{II}(o-TMA)]$^{4+}$.[25] We expect that this result is general, independent of the DFT model.

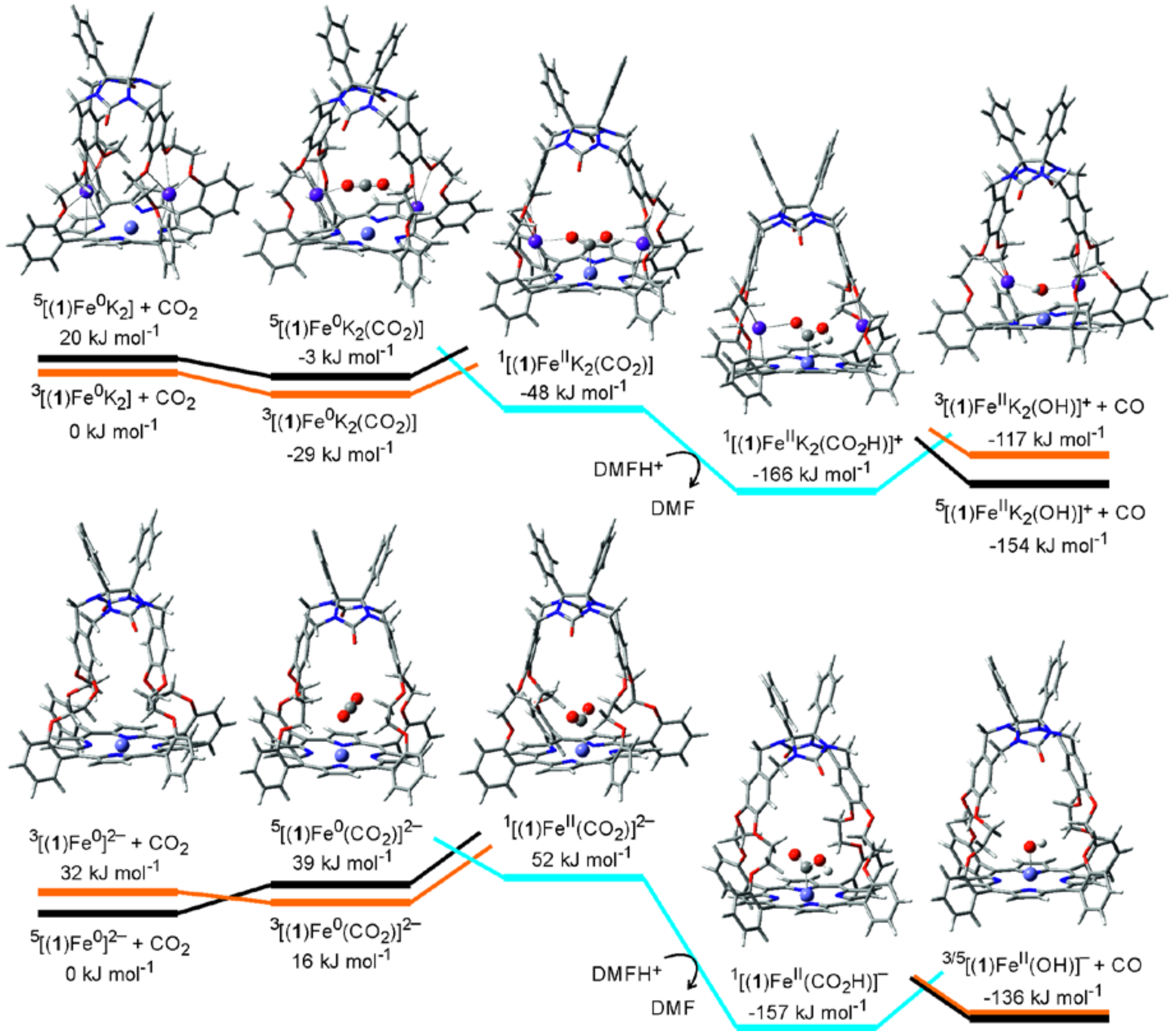

Figure 5. Potential energy surfaces (M06L-D3/def2SVP, SMD solvation model for DMF) for reaction of [(**1**)Fe^{0}K$_2$] (top) and [(**1**)Fe^{0}]$^{2-}$ (bottom) with CO$_2$, respectively. The energies are Gibbs free energies at 298 K and 1 atm in the DMF solvation model. Enthalpies at 0 K and 298 K as well as the optimized geometries are in the Supporting Information (Figure S24). The positions of Fe, K, and CO$_2$ are highlighted by using ball and stick presentation. The depicted structures correspond to the given ground states. The energy levels are spin-state color-coded: blue = singlet, orange = triplet, black = quintet.

CONCLUSIONS

The iron porphyrin glycoluril-based cage complex [(**1**)Fe] offers a constrained reaction site that promotes electrochemical reduction of CO_2 to CO with a selectivity that is largely superior to that of the reference iron tetraphenylporphyrin complex. In addition, we show that the host-guest chemistry of the cage can be used to modify the electronic properties of the metal center. The oxyethyleneoxy functions attached to the side walls of the cage catalyst are optimal for hosting the potassium ions, which opens the possibility to use the electrolyte containing this ion for tuning the electronic properties of the catalyst. The immobilized iron cage catalyst [(**1**)Fe]@carbon has both a higher activity and a higher selectivity for CO_2RR at a 96 mV reduced overpotential in the $KHCO_3$-based electrolyte than the reference catalyst [Fe(TPP)]@carbon. The combination of electrochemistry and electrospray ionization mass spectrometry allowed us to detect the key intermediates of the reaction, i.e. $[(\mathbf{1})Fe^{II}(CO_2H)K_2]^+$ and $[(\mathbf{1})Fe^{II}(CO_2H)]^-$. Both intermediates decompose by the elimination of CO, yielding iron(II)hydroxo complexes with a similar activation energy. The structure of the $[(\mathbf{1})Fe^{II}(CO_2H)K_2]^+$ intermediate including the details of the potassium binding was unraveled by cryogenic ion spectroscopy of the isolated ions. DFT calculations showed that the favorable electrostatic potential formed by the potassium ions make all steps of CO_2RR exoergic. Especially, the key step of 2-electron reduction to form the Fe^{II}-COO^- intermediate is endothermic for $[(\mathbf{1})Fe(CO_2)]^{2-}$, but becomes exothermic for $[(\mathbf{1})Fe^{II}(CO_2)K_2]$.

EXPERIMENTAL AND COMPUTATIONAL DETAILS

Materials. Chemicals were obtained from commercial sources. The diphenylglycoluril-based cage ligand $\mathbf{1}H_2$ was prepared according to the published procedure.[56] The iron complex $[(\mathbf{1})Fe^{III}Cl]$ was prepared using a common procedure with $[FeCl_2(H_2O)_4]$ and characterized (UV-vis ($CHCl_3$) λ_{max}, nm (ε): 416 (3.07×10^5 L·mol^{-1}·cm^{-1}), 510 (3.81×10^4 L·mol^{-1}·cm^{-1}), 574 (1.30×10^4 L·mol^{-1}·cm^{-1}). Emission ($CHCl_3$, $\lambda_{excitation}$ = 416 nm) λ_{max}, nm: 472, 650, 717. HRMS: calcd. for $[C_{84}H_{62}N_8O_{10}Fe\cdot CH_3OH]^+$ 1430.42037, found 1430.39428.). For more details, see the SI.

Electrochemistry: Homogeneous cyclic voltammetry (CV) experiments were performed using a standard three electrode assembly in a solution of 0.25 mM catalyst, 0.1 M of a supporting electrolyte ($TBABF_4$, $NaBF_4$ and KBF_4) and 0.5 M H_2O in DMF (10 mL). We used a glassy carbon working electrode, a double junction non-aqueous Ag/AgCl reference electrode filled with 2 M LiCl in ethanol as the inner electrolyte, and a platinum mesh of 2 cm^2 area as the counter electrode. The reference electrode was calibrated against the Ferrocene/Ferrocenium redox couple. Prior to the measurements the solution was bubbled with N_2 or CO_2 for 30 minutes and during the measurements the corresponding gas was kept flowing through the head space.

Heterogeneous experiments were performed with the catalyst deposited at the vulcanized carbon black (the optimized mass ratio of carbon to the catalyst was 1:1/6, see the SI for the details of the preparation and the optimization). The catalyst ink (10 µL) was drop-casted on a clean glassy carbon electrode and air dried (using IR lamp). The reference electrode was an aqueous Ag/AgCl reference electrode filled with 3 M KCl. The CVs were recorded in aqueous bicarbonate solution (0.5 M) of different electrolytes ($TEAHCO_3$, $NaHCO_3$, $KHCO_3$) purged either with N_2 or with CO_2 for 30 minutes. A blank experiment performed only with carbon black in $KHCO_3$ did not show any CO_2RR activity (Figure S6). Product analysis was done by performing preparative controlled potential electrolysis (CPE) at different polarization voltages. We used a modified H-cell (Figure S10) with three compartments, working electrode and counter electrode separated by a Nafion proton exchange membrane (activated prior to the assembly), and an additional CO_2 saturation compartment. The saturation compartment was attached to the working electrode through an opening, allowing a free mixing of electrolytes between compartments. Head space of the working electrode was held air tight and connected to an in-line gas chromatograph. The catalyst ink (500 µL) was drop casted (10 µL x 50) on a Toray carbon paper electrode (area = 1 cm^2) and dried in the air (using IR Lamp). The reference electrode (aq. Ag/AgCl-3 M KCl) was placed close to the working electrode. A platinum wire gauze (geometrical area approx. 11 cm^2) was used as the counter electrode. The head space of the cathode compartment was calibrated injecting known volumes CO and H_2. Before the measurement, electrolyte was deoxygenated with N_2 purging and then saturated with CO_2. The CO_2 bubbling was continued in the saturation compartment and the electrolyte was stirred during the measurement (10 min). The gaseous products from the cathode head space were analysed by the in-line GC (see more details in the SI). An extended electrolysis for 2 hrs at -1.4 V (vs. Ag/AgCl) and subsequent NMR analysis was performed to check the possible formation of liquid products.

Mass spectrometry. ESI-MS spectra were measured with a LCQ mass spectrometer (a Paul-type ion trap) connected through a silica capillary to a gas-tight, small volume single compartment electrochemical cell with three electrode assembly (a stainless-steel counter electrode, a Pt wire reference electrode - pseudo-reference electrode, and a Toray carbon working electrode). The silica capillary was sandwiched in between two Toray carbon sheets of the working electrode. The electrochemically generated species on the surface of the working electrode were transferred with the capillary (using N_2/CO_2 overpressure in the cell) to the mass spectrometer. The polarization of the electrode was controlled using a USB powered potentiostat (Ivium pocketSTAT2). The interference from the high voltage of ESI source was eliminated by operating potentiostat without a ground connection (floating). A 5 kV USB isolator was used between the connection to the computer to decouple the potentiostat from the ground contact (see the SI for further details). The solutions consisted of the cage catalyst (0.8 mg) dissolved in 0.5 mL of DCM and diluted to 4 mL with ACN to a final concentration of 143 µM with addition of the KBF_4 salt (150 µM) serving as both supporting electrolyte and K^+ ion source (see more details and results in the SI, Figure S14).

Ion spectroscopy. The helium tagging infrared photodissociation (IRPD) spectra were measured with the ISORI instrument.[48,57] The ions were generated in the same way as for the electrochemistry mass spectrometry study. The ions of interest were mass-selected by a quadrupole mass filter and guided to a cold ion trap (~10 K) by an octopole ion guide. The ions were trapped and thermalized in collisions with helium buffer gas. The cold ions formed complexes with helium MHe^+ that were used for monitoring IR photon absorption. The trapped ions were irradiated by a tuneable NdYAG laser pumped OPO/OPA system (Laser Vision). After the irradiation, the ions were extracted from the trap, mass-analysed by a quadrupole and detected with a Daly-type detector working in the counting mode. The absorption of given photons (ν_i) was monitored as a depletion of the number of the MHe^+ complexes (N_0). The spectrum is plotted as $1-N(\nu_i)/N_0$, where $N(\nu_i)$ and N_0 were measured in alternating cycles with or without the laser beam admitted to the trap (for more details, see the SI).

DFT calculations. The preliminary calculations (Figure 1) were performed in the gas phase using the M06L functional[58] with the D3 dispersion[59] correction and with the def2SVP basis set[60] as implemented in the Gaussian program. The exploration of the mechanism (Figure 5) was performed at the same level but including the SMD solvation model for DMF (N,N-dimethylformamide). The relative Gibbs energies were corrected for the change in the number of the moles (n) in a reaction step by a correction of ($7.9\ \Delta n$) kJ mol^{-1}. The relative energies at 0K are in Figure S24. The IRPD spectra are compared to the harmonic theoretical IR spectra calculated in the gas phase at the B3LYP-D3/def2SVP of theory.[61–63] The scaling factor is 0.978. All reported results are for the minima on the potential energy surfaces as verified by the Hessian calculations.

ASSOCIATED CONTENT

Supporting Information

Further experimental and theoretical details, all electrochemistry results, details of the experiments and their analysis, the details of the electrochemistry setup for bridging with electrospray ionization, experimental and calculated spectra, theoretical results in the gas phase, calculated structures (in XYZ format) This material is available free of charge via the Internet at http://pubs.acs.org.

AUTHOR INFORMATION

Corresponding Author

*j.roithova@science.ru.nl

Notes

The authors declare no competing financial interests.

ACKNOWLEDGMENT

The work was supported by the Netherlands Organization for Scientific Research (NWO, 740.018.022 and VI.C.192.044) and through the HRMC fellowship to E.P.

References

(1) Ampelli, C.; Perathoner, S.; Centi, G. CO 2 Utilization: An Enabling Element to Move to a Resource- and Energy-Efficient Chemical and Fuel Production. *Philos. Trans. R. Soc. A Math. Phys. Eng. Sci.* **2015**, *373* (2037), 20140177. https://doi.org/10.1098/rsta.2014.0177.

(2) Chen, C.; Khosrowabadi Kotyk, J. F.; Sheehan, S. W. Progress toward Commercial Application of Electrochemical Carbon Dioxide Reduction. *Chem* **2018**, *4* (11), 2571–2586. https://doi.org/10.1016/j.chempr.2018.08.019.

(3) Francke, R.; Schille, B.; Roemelt, M. Homogeneously Catalyzed Electroreduction of Carbon Dioxide—Methods, Mechanisms, and Catalysts. *Chem. Rev.* **2018**, *118* (9), 4631–4701. https://doi.org/10.1021/acs.chemrev.7b00459.

(4) Garg, S.; Li, M.; Weber, A. Z.; Ge, L.; Li, L.; Rudolph, V.; Wang, G.; Rufford, T. E. Advances and Challenges in Electrochemical CO 2 Reduction Processes: An Engineering and Design Perspective Looking beyond New Catalyst Materials. *J. Mater. Chem. A* **2020**, *8* (4), 1511–1544. https://doi.org/10.1039/C9TA13298H.

(5) Jin, S.; Hao, Z.; Zhang, K.; Yan, Z.; Chen, J. Advances and Challenges for the Electrochemical Reduction of CO 2 to CO: From Fundamentals to Industrialization. *Angew. Chemie Int. Ed.* **2021**, *60* (38), 20627–20648. https://doi.org/10.1002/anie.202101818.

(6) Birdja, Y. Y.; Pérez-Gallent, E.; Figueiredo, M. C.; Göttle, A. J.; Calle-Vallejo, F.; Koper, M. T. M. Advances and Challenges in Understanding the Electrocatalytic Conversion of Carbon Dioxide to Fuels. *Nat. Energy* **2019**, *4* (9), 732–745. https://doi.org/10.1038/s41560-019-0450-y.

(7) Johnson, D.; Qiao, Z.; Djire, A. Progress and Challenges of Carbon Dioxide Reduction Reaction on Transition Metal Based Electrocatalysts. *ACS Appl. Energy Mater.* **2021**, *4* (9), 8661–8684. https://doi.org/10.1021/acsaem.1c01624.

(8) Corbin, N.; Zeng, J.; Williams, K.; Manthiram, K. Heterogeneous Molecular Catalysts for Electrocatalytic CO2 Reduction. *Nano Res.* **2019**, *12* (9), 2093–2125. https://doi.org/10.1007/s12274-019-2403-y.

(9) Liu, A.; Gao, M.; Ren, X.; Meng, F.; Yang, Y.; Gao, L.; Yang, Q.; Ma, T. Current Progress in Electrocatalytic Carbon Dioxide Reduction to Fuels on Heterogeneous Catalysts. *J. Mater. Chem. A* **2020**, *8* (7), 3541–3562. https://doi.org/10.1039/C9TA11966C.

(10) Kornienko, N.; Zhao, Y.; Kley, C. S.; Zhu, C.; Kim, D.; Lin, S.; Chang, C. J.; Yaghi, O. M.; Yang, P. Metal-Organic Frameworks for Electrocatalytic Reduction of Carbon Dioxide. *J. Am. Chem. Soc.* **2015**, *137* (44), 14129–14135. https://doi.org/10.1021/jacs.5b08212.

(11) Li, X.; Wang, S.; Li, L.; Sun, Y.; Xie, Y. Progress and Perspective for In Situ Studies of CO 2 Reduction. *J. Am. Chem. Soc.* **2020**, *142* (21), 9567–9581. https://doi.org/10.1021/jacs.0c02973.

(12) Zhu, Q.; Murphy, C. J.; Baker, L. R. Opportunities for Electrocatalytic CO 2 Reduction

Enabled by Surface Ligands. *J. Am. Chem. Soc.* **2022**, *144* (7), 2829–2840. https://doi.org/10.1021/jacs.1c11500.

(13) Elouarzaki, K.; Kannan, V.; Jose, V.; Sabharwal, H. S.; Lee, J. M. Recent Trends, Benchmarking, and Challenges of Electrochemical Reduction of CO2 by Molecular Catalysts. *Adv. Energy Mater.* **2019**, *9* (24), 1–33. https://doi.org/10.1002/aenm.201900090.

(14) Boutin, E.; Merakeb, L.; Ma, B.; Boudy, B.; Wang, M.; Bonin, J.; Anxolabéhère-Mallart, E.; Robert, M. Molecular Catalysis of CO2reduction: Recent Advances and Perspectives in Electrochemical and Light-Driven Processes with Selected Fe, Ni and Co Aza Macrocyclic and Polypyridine Complexes. *Chem. Soc. Rev.* **2020**, *49* (16), 5772–5809. https://doi.org/10.1039/d0cs00218f.

(15) Costentin, C.; Robert, M.; Savéant, J.-M.; Tatin, A. Efficient and Selective Molecular Catalyst for the CO2 -to-CO Electrochemical Conversion in Water. *Proc. Natl. Acad. Sci.* **2015**, *112* (22), 6882–6886. https://doi.org/10.1073/pnas.1507063112.

(16) Barrett, A. J. A.; Brunner, B. F. M.; Cheung, C. P. L.; Kubiak, D. C. P.; Lee, E. G. L.; Miller, F. C. J.; Waldie, G. K. M.; Zhanaidarova, H. A. Chapter 1. Approaches to Controlling Homogeneous Electrochemical Reduction of Carbon Dioxide. In *RSC Energy and Environment Series*; 2020; Vol. 2021-Janua, pp 1–66. https://doi.org/10.1039/9781788015844-00001.

(17) Wang, J.; Dou, S.; Wang, X. Structural Tuning of Heterogeneous Molecular Catalysts for Electrochemical Energy Conversion. *Sci. Adv.* **2021**, *7* (13), 1–14. https://doi.org/10.1126/sciadv.abf3989.

(18) Jayathilake, B. S.; Bhattacharya, S.; Vaidehi, N.; Narayanan, S. R. Efficient and Selective Electrochemically Driven Enzyme-Catalyzed Reduction of Carbon Dioxide to Formate Using Formate Dehydrogenase and an Artificial Cofactor. *Acc. Chem. Res.* **2019**, *52* (3), 676–685. https://doi.org/10.1021/acs.accounts.8b00551.

(19) Contaldo, U.; Guigliarelli, B.; Perard, J.; Rinaldi, C.; Le Goff, A.; Cavazza, C. Efficient Electrochemical CO2 /CO Interconversion by an Engineered Carbon Monoxide Dehydrogenase on a Gas-Diffusion Carbon Nanotube-Based Bioelectrode. *ACS Catal.* **2021**, *11* (9), 5808–5817. https://doi.org/10.1021/acscatal.0c05437.

(20) Stoffel, G. M. M.; Saez, D. A.; DeMirci, H.; Vögeli, B.; Rao, Y.; Zarzycki, J.; Yoshikuni, Y.; Wakatsuki, S.; Vöhringer-Martinez, E.; Erb, T. J. Four Amino Acids Define the CO 2 Binding Pocket of Enoyl-CoA Carboxylases/Reductases. *Proc. Natl. Acad. Sci.* **2019**, *116* (28), 13964–13969. https://doi.org/10.1073/pnas.1901471116.

(21) Smith, P. T.; Benke, B. P.; Cao, Z.; Kim, Y.; Nichols, E. M.; Kim, K.; Chang, C. J. Iron Porphyrins Embedded into a Supramolecular Porous Organic Cage for Electrochemical CO2 Reduction in Water. *Angew. Chemie Int. Ed.* **2018**, *57* (31), 9684–9688. https://doi.org/10.1002/anie.201803873.

(22) Chen, Y.; Li, P.; Noh, H.; Kung, C.-W.; Buru, C. T.; Wang, X.; Zhang, X.; Farha, O. K. Stabilization of Formate Dehydrogenase in a Metal–Organic Framework for Bioelectrocatalytic Reduction of CO2. *Angew. Chemie* **2019**, *131* (23), 7764–7768. https://doi.org/10.1002/ange.201901981.

(23) Liu, D.-C.; Wang, H.-J.; Wang, J.-W.; Zhong, D.-C.; Jiang, L.; Lu, T.-B. Highly Efficient and Selective Visible-Light Driven CO2 -to-CO Conversion by a Co-Based Cryptate in H2O/CH3CN Solution. *Chem. Commun.* **2018**, *54* (80), 11308–11311. https://doi.org/10.1039/C8CC04892D.

(24) Margarit, C. G.; Schnedermann, C.; Asimow, N. G.; Nocera, D. G. Carbon Dioxide Reduction by Iron Hangman Porphyrins. *Organometallics* **2019**, *38* (6), 1219–1223. https://doi.org/10.1021/acs.organomet.8b00334.

(25) Azcarate, I.; Costentin, C.; Robert, M.; Savéant, J.-M. Through-Space Charge Interaction Substituent Effects in Molecular Catalysis Leading to the Design of the Most Efficient Catalyst of CO2 -to-CO Electrochemical Conversion. *J. Am. Chem. Soc.* **2016**, *138* (51), 16639–16644. https://doi.org/10.1021/jacs.6b07014.

(26) Hessenauer-Ilicheva, N.; Franke, A.; Meyer, D.; Woggon, W.-D.; van Eldik, R. Mechanistic Insight into Formation of Oxo-Iron(IV) Porphyrin π-Cation Radicals from Enzyme Mimics of Cytochrome P450 in Organic Solvents. *Chem. - A Eur. J.* **2009**, *15* (12), 2941–2959. https://doi.org/10.1002/chem.200801423.

(27) Gotico, P.; Halime, Z.; Aukauloo, A. Recent Advances in Metalloporphyrin-Based Catalyst Design towards Carbon Dioxide Reduction: From Bio-Inspired Second Coordination Sphere Modifications to Hierarchical Architectures. *Dalt. Trans.* **2020**, *49* (8), 2381–2396. https://doi.org/10.1039/C9DT04709C.

(28) Martin, D. J.; Mayer, J. M. Oriented Electrostatic Effects on O2 and CO2 Reduction by a Polycationic Iron Porphyrin. *J. Am. Chem. Soc.* **2021**, *143* (30), 11423–11434. https://doi.org/10.1021/jacs.1c03132.

(29) Hong, D.; Kawanishi, T.; Tsukakoshi, Y.; Kotani, H.; Ishizuka, T.; Kojima, T. Efficient Photocatalytic CO2 Reduction by a Ni(II) Complex Having Pyridine Pendants through Capturing a Mg2+ Ion as a Lewis-Acid Cocatalyst. *J. Am. Chem. Soc.* **2019**, *141* (51), 20309–20317. https://doi.org/10.1021/jacs.9b10597.

(30) Elemans, J. A. A. W.; Nolte, R. J. M. Porphyrin Cage Compounds Based on Glycoluril – from Enzyme Mimics to Functional Molecular Machines. *Chem. Commun.* **2019**, *55* (65), 9590–9605. https://doi.org/10.1039/C9CC04372A.

(31) Bullock, R. M.; Das, A. K.; Appel, A. M. Surface Immobilization of Molecular Electrocatalysts for Energy Conversion. *Chem. - A Eur. J.* **2017**, *23* (32), 7626–7641. https://doi.org/10.1002/chem.201605066.

(32) Sun, L.; Reddu, V.; Fisher, A. C.; Wang, X. Electrocatalytic Reduction of Carbon Dioxide: Opportunities with Heterogeneous Molecular Catalysts. *Energy Environ. Sci.* **2020**, *13* (2), 374–403. https://doi.org/10.1039/C9EE03660A.

(33) Maurin, A.; Robert, M. Catalytic CO 2 -to-CO Conversion in Water by Covalently Functionalized Carbon Nanotubes with a Molecular Iron Catalyst. *Chem. Commun.* **2016**, *52* (81), 12084–12087. https://doi.org/10.1039/C6CC05430G.

(34) Rudnev, A. V.; Zhumaev, U. E.; Kuzume, A.; Vesztergom, S.; Furrer, J.; Broekmann, P.; Wandlowski, T. The Promoting Effect of Water on the Electroreduction of CO2 in Acetonitrile. *Electrochim. Acta* **2016**, *189*, 38–44.

https://doi.org/10.1016/j.electacta.2015.12.088.

(35) Moura de Salles Pupo, M.; Kortlever, R. Electrolyte Effects on the Electrochemical Reduction of CO2. *ChemPhysChem* **2019**, *20* (22), 2926–2935. https://doi.org/10.1002/cphc.201900680.

(36) Nitopi, S.; Bertheussen, E.; Scott, S. B.; Liu, X.; Engstfeld, A. K.; Horch, S.; Seger, B.; Stephens, I. E. L.; Chan, K.; Hahn, C.; et al. Progress and Perspectives of Electrochemical CO2 Reduction on Copper in Aqueous Electrolyte. *Chem. Rev.* **2019**, *119* (12), 7610–7672. https://doi.org/10.1021/acs.chemrev.8b00705.

(37) Mehara, J.; Roithová, J. Identifying Reactive Intermediates by Mass Spectrometry. *Chem. Sci.* **2020**, *11* (44), 11960–11972. https://doi.org/10.1039/D0SC04754F.

(38) Liu, J.; Yu, K.; Zhang, H.; He, J.; Jiang, J.; Luo, H. Mass Spectrometric Detection of Fleeting Neutral Intermediates Generated in Electrochemical Reactions. *Chem. Sci.* **2021**, *12* (27), 9494–9499. https://doi.org/10.1039/D1SC01385H.

(39) Herl, T.; Matysik, F.-M. Recent Developments in Electrochemistry–Mass Spectrometry. *ChemElectroChem* **2020**, *7* (12), 2498–2512. https://doi.org/10.1002/celc.202000442.

(40) Oberacher, H.; Pitterl, F.; Erb, R.; Plattner, S. Mass Spectrometric Methods for Monitoring Redox Processes in Electrochemical Cells. *Mass Spectrom. Rev.* **2015**, *34* (1), 64–92. https://doi.org/10.1002/mas.21409.

(41) Wang, Z.; Zhang, Y.; Liu, B.; Wu, K.; Thevuthasan, S.; Baer, D. R.; Zhu, Z.; Yu, X.-Y.; Wang, F. In Situ Mass Spectrometric Monitoring of the Dynamic Electrochemical Process at the Electrode–Electrolyte Interface: A SIMS Approach. *Anal. Chem.* **2017**, *89* (1), 960–965. https://doi.org/10.1021/acs.analchem.6b04189.

(42) Miller, T. M. Thermal Electron Attachment and Detachment in Gases. In *Advances in Atomic, Molecular and Optical Physics*; Elsevier Masson SAS, 2005; Vol. 51, pp 299–342. https://doi.org/10.1016/S1049-250X(05)51018-8.

(43) Zins, E.-L.; Pepe, C.; Schröder, D. Energy-Dependent Dissociation of Benzylpyridinium Ions in an Ion-Trap Mass Spectrometer. *J. Mass Spectrom.* **2010**, *45* (11), 1253–1260. https://doi.org/10.1002/jms.1847.

(44) Rahrt, R.; Auth, T.; Demireva, M.; Armentrout, P. B.; Koszinowski, K. Benzhydrylpyridinium Ions: A New Class of Thermometer Ions for the Characterization of Electrospray-Ionization Mass Spectrometers. *Anal. Chem.* **2019**, *91* (18), 11703–11711. https://doi.org/10.1021/acs.analchem.9b02257.

(45) Mondal, B.; Rana, A.; Sen, P.; Dey, A. Intermediates Involved in the 2e – /2H + Reduction of CO2 to CO by Iron(0) Porphyrin. *J. Am. Chem. Soc.* **2015**, *137* (35), 11214–11217. https://doi.org/10.1021/jacs.5b05992.

(46) Costentin, C.; Drouet, S.; Passard, G.; Robert, M.; Savéant, J.-M. Proton-Coupled Electron Transfer Cleavage of Heavy-Atom Bonds in Electrocatalytic Processes. Cleavage of a C–O Bond in the Catalyzed Electrochemical Reduction of CO2. *J. Am. Chem. Soc.* **2013**, *135* (24), 9023–9031. https://doi.org/10.1021/ja4030148.

(47) Fukuzumi, S.; Lee, Y.-M.; Ahn, H. S.; Nam, W. Mechanisms of Catalytic Reduction of CO2 with Heme and Nonheme Metal Complexes. *Chem. Sci.* **2018**, *9* (28), 6017–6034. https://doi.org/10.1039/C8SC02220H.

(48) Roithová, J.; Gray, A.; Andris, E.; Jašík, J.; Gerlich, D. Helium Tagging Infrared Photodissociation Spectroscopy of Reactive Ions. *Acc. Chem. Res.* **2016**, *49* (2), 223–230. https://doi.org/10.1021/acs.accounts.5b00489.

(49) Jašík, J.; Žabka, J.; Roithová, J.; Gerlich, D. Infrared Spectroscopy of Trapped Molecular Dications below 4K. *Int. J. Mass Spectrom.* **2013**, *354–355*, 204–210. https://doi.org/10.1016/j.ijms.2013.06.007.

(50) Menges, F. S.; Craig, S. M.; Tötsch, N.; Bloomfield, A.; Ghosh, S.; Krüger, H.-J.; Johnson, M. A. Capture of CO 2 by a Cationic Nickel(I) Complex in the Gas Phase and Characterization of the Bound, Activated CO 2 Molecule by Cryogenic Ion Vibrational Predissociation Spectroscopy. *Angew. Chemie Int. Ed.* **2016**, *55* (4), 1282–1285. https://doi.org/10.1002/anie.201507965.

(51) Iskra, A.; Gentleman, A. S.; Cunningham, E. M.; Mackenzie, S. R. Carbon Dioxide Binding to Metal Oxides: Infrared Spectroscopy of NbO2+(CO2) and TaO2+(CO2) Complexes. *Int. J. Mass Spectrom.* **2019**, *435*, 93–100. https://doi.org/10.1016/j.ijms.2018.09.038.

(52) Dodson, L. G.; Thompson, M. C.; Weber, J. M. Characterization of Intermediate Oxidation States in CO 2 Activation. *Annu. Rev. Phys. Chem.* **2018**, *69* (1), 231–252. https://doi.org/10.1146/annurev-physchem-050317-021122.

(53) Amanullah, S.; Saha, P.; Dey, A. Activating the Fe(I) State of Iron Porphyrinoid with Second-Sphere Proton Transfer Residues for Selective Reduction of CO 2 to HCOOH via Fe(III/II)–COOH Intermediate(S). *J. Am. Chem. Soc.* **2021**, *143* (34), 13579–13592. https://doi.org/10.1021/jacs.1c04392.

(54) Römelt, C.; Song, J.; Tarrago, M.; Rees, J. A.; van Gastel, M.; Weyhermüller, T.; DeBeer, S.; Bill, E.; Neese, F.; Ye, S. Electronic Structure of a Formal Iron(0) Porphyrin Complex Relevant to CO 2 Reduction. *Inorg. Chem.* **2017**, *56* (8), 4745–4750. https://doi.org/10.1021/acs.inorgchem.7b00401.

(55) Davethu, P. A.; De Visser, S. P. CO2 Reduction on an Iron-Porphyrin Center: A Computational Study. *J. Phys. Chem. A* **2019**, *123* (30), 6527–6535. https://doi.org/10.1021/acs.jpca.9b05102.

(56) Gilissen, P. J.; Swartjes, A.; Spierenburg, B.; Bruekers, J. P. J.; Tinnemans, P.; White, P. B.; Rutjes, F. P. J. T.; Nolte, R. J. M.; Elemans, J. A. A. W. Rapid and Scalable Synthesis of Chiral Porphyrin Cage Compounds. *Tetrahedron* **2019**, *75* (33), 4640–4647. https://doi.org/10.1016/j.tet.2019.07.009.

(57) Gerlich, D.; Jašík, J.; Roithová, J. Tagging Fullerene Ions with Helium in a Cryogenic Quadrupole Trap. *Int. J. Mass Spectrom.* **2019**, *438*, 78–86. https://doi.org/10.1016/j.ijms.2018.12.018.

(58) Zhao, Y.; Truhlar, D. G. A New Local Density Functional for Main-Group Thermochemistry, Transition Metal Bonding, Thermochemical Kinetics, and

Noncovalent Interactions. *J. Chem. Phys.* **2006**, *125* (19), 194101. https://doi.org/10.1063/1.2370993.

(59) Grimme, S.; Antony, J.; Ehrlich, S.; Krieg, H. A Consistent and Accurate Ab Initio Parametrization of Density Functional Dispersion Correction (DFT-D) for the 94 Elements H-Pu. *J. Chem. Phys.* **2010**, *132* (15), 154104. https://doi.org/10.1063/1.3382344.

(60) Weigend, F.; Ahlrichs, R. Balanced Basis Sets of Split Valence, Triple Zeta Valence and Quadruple Zeta Valence Quality for H to Rn: Design and Assessment of Accuracy. *Phys. Chem. Chem. Phys.* **2005**, *7* (18), 3297. https://doi.org/10.1039/b508541a.

(61) Becke, A. D. Density-functional Thermochemistry. III. The Role of Exact Exchange. *J. Chem. Phys.* **1993**, *98* (7), 5648–5652. https://doi.org/10.1063/1.464913.

(62) Lee, C.; Yang, W.; Parr, R. G. Development of the Colle-Salvetti Correlation-Energy Formula into a Functional of the Electron Density. *Phys. Rev. B* **1988**, *37* (2), 785–789. https://doi.org/10.1103/PhysRevB.37.785.

(63) Miehlich, B.; Savin, A.; Stoll, H.; Preuss, H. Results Obtained with the Correlation Energy Density Functionals of Becke and Lee, Yang and Parr. *Chem. Phys. Lett.* **1989**, *157* (3), 200–206. https://doi.org/10.1016/0009-2614(89)87234-3.